The improved output performance of a broad-area vertical-cavity surface-emitting laser with an optimized electrode diameter

2013 Chinese Phys. B 22 064209

(http://iopscience.iop.org/1674-1056/22/6/064209)

The improved output performance of a broad-area vertical-cavity surface-emitting laser with an optimized electrode diameter*

Zhang Xing(张 星), Ning Yong-Qiang(宁永强)†, Qin Li(秦 莉),
Tong Cun-Zhu(佟存柱), Liu Yun(刘 云), and Wang Li-Jun(王立军)

State Key Laboratory of Luminescence and Applications, Changchun Institute of Optics, Fine Mechanics and Physics, Chinese Academy of Sciences, Changchun 130033, *China*

(Received 24 October 2012; revised manuscript received 4 January 2013)

The output performance of a 980-nm broad-area vertical-cavity surface-emitting laser (VCSEL) is improved by optimizing the p-electrode diameter in this study. Based on a three-dimensional finite-element method, the current density distribution within the active region of the VCSEL is optimized through the appropriate adjustment of the p-electrode diameter, and uniform current-density distribution is achieved. Then, the effects of this optimization are studied experimentally. The *L–I–V* characteristics under different temperatures of the VCSELs with different p-electrode diameters are investigated, and better temperature stability is demonstrated in the VCSEL with an optimized p-electrode diameter. The far-field measurements show that with an injected current of 2 A, the far-field divergence angle of the VCSEL with an optimized p-electrode diameter is 9°, which is much lower than the far-field angle of the VCSEL without this optimization. Also the VCSEL with an optimized p-electrode diameter shows a better near-field distribution.

Keywords: vertical-cavity surface-emitting lasers, finite-element analysis, far-field divergence, near-field distribution

PACS: 42.55.Px **DOI:** 10.1088/1674-1056/22/6/064209

1. Introduction

The vertical-cavity surface-emitting laser (VCSEL) has a unique cavity geometry that offers numerous advantages, such as a circular beam spot, a single longitudinal mode, easy formation of a two-dimensional (2D) array, and integratability with electronic devicea, in comparison to edge-emitting semiconductor lasers (EELs).[1–5] Unlike EELs, VCSELs do not suffer from catastrophic optical damage (COD), which means that VCSELs can be operated reliably at higher temperatures, making them suitable for some high-power applications.[6] High-power VCSELs have shown their great application potential in treating solid-state materials, free-space communication, and laser pumping. Researchers have made great efforts to improve the device performances of high-power VCSELs.[7–12]

To enhance the output power of VCSELs for high-power application, one can simply increase the diameter of the active region in a single device or arrange the VCSEL in a 2D array,[7] that is, the total lasing area is enlarged. However, a larger lasing area will cause the so-called current self-distribution (CSD) effect.[13] The CSD effect can cause a drastic increase of beam divergence and a nonuniform self-heating effect, which, in turn, lowers the beam quality and reduces the reliability. Angelos *et al.*[14] investigated the current-spreading mechanism in a bottom-emitting VCSEL and theoretically analyzed the relationship between current-injection structure and device performance. Yan *et al.*[15] used filter apertures to suppress the side lobes, which are caused by the CSD effect, in the far-field distribution of a broad-area VCSEL. However, the filter aperture cannot actually solve the problem of nonuniform current-density distribution. There have been many other studies on the current injection of VCSEL devices, such as investigating the relationship between current injection and wall-plug efficiency[16,17] or the thermal behavior[18–20] of VCSEL devices. However, how to eliminate the CSD effect was not mentioned in those studies.

Recently, we demonstrated that the adjustment of electrode diameter is helpful to solve the CSD problem and a significant suppression of divergence was achieved using this method.[21,22] However, a systematic experimental and theoretical study on this approach has not been presented previously. To explore the full potential of this approach, a deep insight into the characteristics such as *L–I–V*, temperature characteristics, and near-field distribution of this device is necessary. In this work, to improve the output performance in a broad-area VCSEL through electrode optimization, the influences of the p-electrode diameter on the *L–I–V* and temperature characteristics, near- and far-field distributions are investigated in detail. First, a three-dimensional (3D) finite-element model is built to simulate the steady-state current-density distribution. The influence of the p-electrode diameter on the current-density distribution is analyzed. Second, VCSEL sin-

*Project supported by the National Natural Science Foundation of China (Grant Nos. 61204056, 61234004, 90923037, and 11074247) and the Jilin Provincial Science and Technology Development Plan Item (Grant Nos. 201105025 and 20116011).

†Corresponding author. E-mail: ningyq@ciomp.ac.cn

gle devices with different p-electrode diameters are fabricated. Finally, the near- and far-field distributions of these VCSELs are investigated, in addition to the *L–I–V* and temperature characteristics, the optimum p-electrode diameter is found to improve the device performance.

2. VCSEL structure and current-spreading mechanism

2.1. Device structure

The device studied here is a bottom-emitting VCSEL that emits at a resonance wavelength of approximately 980 nm. The schematic diagram of the device structure is shown in Fig. 1. The bottom-emitting structure is chosen because it has been previously shown to provide relatively homogenous current injection for the broad-area high-power VCSEL devices and is suited to sophisticated mounting techniques.[6] The p-doped distributed Bragg reflector (DBR) or p-DBR consists of 30 pairs of $Al_{0.12}Ga_{0.88}As$–$Al_{0.9}Ga_{0.1}As$ layers, and the n-doped DBR (n-DBR) consists of 28.5 pairs of $Al_{0.12}Ga_{0.88}As$–$Al_{0.9}Ga_{0.1}As$ layers. The active region comprises three $In_{0.2}Ga_{0.8}As$–$GaAs_{0.92}P_{0.08}$ quantum wells. Two $Al_{0.2}Ga_{0.8}As$ spacer layers are used to form a $1-\lambda$ resonant cavity. The oxide aperture is formed by selective oxidation between the p-doped spacer layer and the p-DBR to achieve effective carrier and photon confinement.

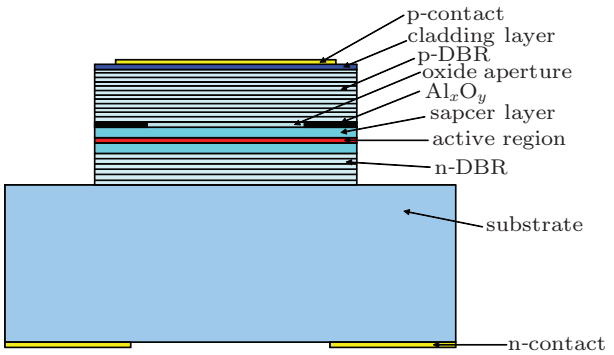

Fig. 1. (color online) Schematic diagram of a 980-nm bottom-emitting VCSEL.

2.2. Current-spreading mechanism

In contrast to the EEL, the current-spreading mechanism in a VCSEL is more complex. The current-spreading mode in EEL is one-dimensional (1D), whereas in a VCSEL, it is 2D. We must consider the current-spreading mechanism in the transverse and the longitudinal direction.

Under steady-state conditions, the electrical potential in a VCSEL is determined by Laplace's equation as

$$\nabla \cdot (\sigma \cdot \nabla \cdot U) = 0. \tag{1}$$

The electrical conductivity, σ, in Eq. (1) is defined by the following vector matrix:

$$\sigma = \begin{pmatrix} \sigma_x & 0 & 0 \\ 0 & \sigma_y & 0 \\ 0 & 0 & \sigma_z \end{pmatrix}, \tag{2}$$

where σ_x, σ_y, and σ_z are determined as follows:

$$\sigma_x = \sigma_y = \frac{\sum \sigma_i d_i}{\sum d_i}, \tag{3}$$

$$\sigma_z = \frac{J_c d_r}{V}. \tag{4}$$

Here, σ_x, σ_y, and σ_z represent the electrical conductivities in the x, y, and z directions, respectively. σ_i in Eq. (3) represents the electrical conductivity of the i-th layer; J_c in Eq. (4) denotes the 1D current density in a region; V refers to the voltage drop across the region; and d_r and d_i are the thickness values of the region and the i-th layer, respectively. J_c can be calculated using the SimWindows[23] software when a voltage V is applied to a particular region in the multilayer structure.

3. 3D finite-element modeling and analysis

3.1. 3D finite-element modeling

We develop a 3D electrical field analysis model in the ANSYS software (Version 12.0) to calculate the current-density distribution in the active region of the VCSEL. To consider the interface- and boundary-scattering effects of electrons, materials with anisotropic properties are used in the DBR, the active region, and the spacer layer. In Table 1 listed are the parameters of the material used in the simulation. Figure 2 shows the mesh-generated 3D finite-element model. There is a significant variation in the mesh size, which is chosen according to the expected gradient of the calculated quantities: the grid is densest in the active and the DBR regions, whereas it is less dense in the substrate.

Table 1. Material parameters used in the simulation.

	Electrical conductivity/$\Omega\cdot m^{-1}$	Thickness/μm
p-contact	$\sigma_x=\sigma_y=\sigma_z=1\times10^7$	0.2
Cladding layer	$\sigma_x=\sigma_y=\sigma_z=4.23\times10^4$	0.04
p-DBR	$\sigma_x=\sigma_y=5.86\times10^3$	4.641
	$\sigma_z=2.33\times10^2$	
Oxide-aperture	$\sigma_x=\sigma_y=\sigma_z=3.66\times10^3$	0.07
Al_xO_y	$\sigma_x=\sigma_y=\sigma_z=1\times10^{-5}$	0.07
p-spacer layer	$\sigma_x=\sigma_y=2.14\times10^3$	0.127
	$\sigma_z=1.17\times10^2$	
Active region	$\sigma_x=\sigma_y=5.9\times10^2$	0.042
	$\sigma_z=1.2\times10^2$	
n-spacer layer	$\sigma_x=\sigma_y=3.19\times10^3$	0.127
	$\sigma_z=2.14\times10^2$	
n-DBR	$\sigma_x=\sigma_y=5.93\times10^4$	4.409
	$\sigma_z=7.42\times10^3$	
Substrate	$\sigma_x=\sigma_y=\sigma_z=4.5\times10^4$	200
n-contact	$\sigma_x=\sigma_y=\sigma_z=1\times10^7$	1

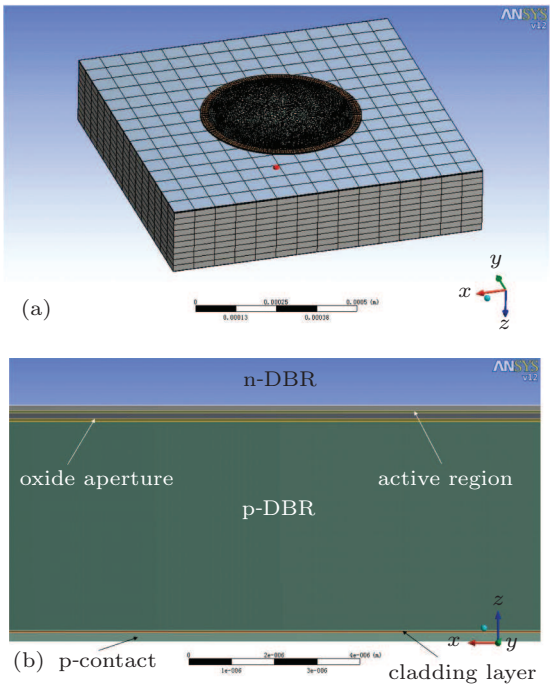

Fig. 2. (color online) (a) 3D model of the VCSEL and the mesh-generated structure. (b) Profile of the model.

3.2. Results of the simulation of current-density distribution

The current-density distribution in the active region of a VCSEL with 450-μm-diameter mesa is simulated. Considering that the operating voltage is 2 V and the flat-band voltage of 980-nm VCSEL device is 1.265 V, a voltage of 0.735 V (the voltage drop across the VCSEL) is applied to the p-electrode. The diameter of the p-electrode is set to be 400 μm, and the oxide-aperture diameters are set to be 450 μm and 400 μm, respectively. From Fig. 3, we can see that the diameter of the active region is governed by the size of the oxide aperture. The existence of the oxide aperture increases the current density in the center of the active region slightly. The CSD effect occurs near the edge of the oxide aperture because the current density increases singificantly in this region, which implies nonuniformity of the current-density distribution. In this case, the threshold will be reached earlier at points near the edge of the oxide aperture, this will cause a ring-shaped output beam and increase the divergence angle drastically.[22]

The current-density distribution of a VCSEL with 400-μm-diameter oxide aperture is shown in Fig. 4. The diameters of the p-electrode are set to be 400, 350, and 300 μm. When the diameter of the p-electrode is smaller, the current density in the center of the active region increases slightly, and the current-density peak near the edge of the oxide aperture is suppressed. Because the diameter of the oxide aperture is relatively constant, the appropriate adjustment of the p-electrode diameter can make the current-density distribution in the active region uniform.

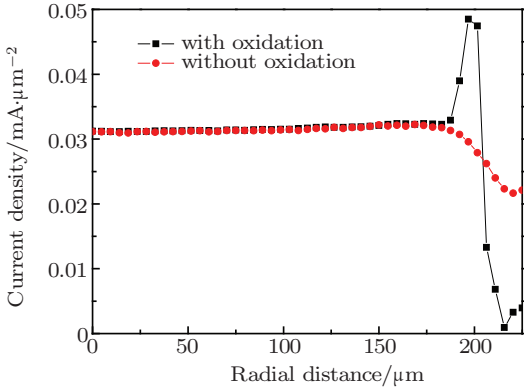

Fig. 3. (color online) Simulated current-density distributions in the active region of the VCSEL, with and without the oxide aperture. The radii of the oxide apertures are set to be 400 μm and 450 μm.

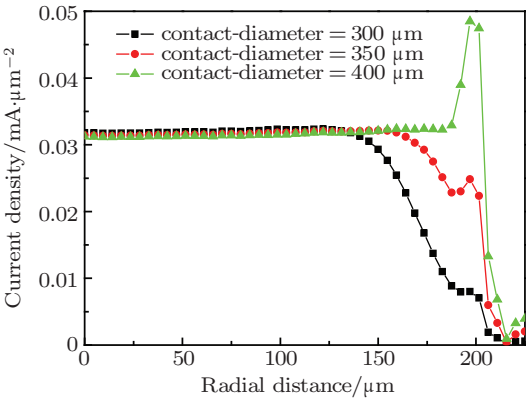

Fig. 4. (color online) Simulated current-density distributions in the active region of VCSELs with p-contact diameters of 300, 350, and 400 μm respectively.

From the simulation results we can see that adjustment of p-electrode is helpful to achieve a uniform current density distribution. However, we still need to determine the optimum diameter of p-electrode for improving the device performance. In the next section, the device characteristics, such as *L*–*I*–*V*, temperature characteristics, and far- and near-field distributions, of the VCSELs with different p-electrode diameters will be investigated experimentally.

4. Experimental investigation

To confirm the optimum p-electrode diameter for improving device performance, three 980-nm broad-area VCSELs with 450-μm-diameter mesa and different p-electrode diameters are fabricated. The device structure is as described in Subsection 2.1. The detailed fabrication process is as follows. Circular mesas are wet-etched chemically on the p-doped side of the wafer. After selective oxidation, SiO_2 is deposited on the surface of the mesa. Then, the SiO_2 on the top side of the mesa is etched away, and the p-electrode is prepared by sputtering Ti/Pt/Au. The thickness of the GaAs substrate is reduced to 200 μm by a mechanical lapping and polishing process. After evaporation of AuGeNi/Au, the output window is

created by the lift-off process, and an antireflection layer is grown in it to avoid back-reflection into the cavity. Finally, the wafer is split into 1-mm × 1-mm chips and In-bonded to a Cu heatsink. Further details of the device structure and output characteristics can be found in Ref. [9]. The diameters of the p-electrodes are 400, 350, and 300 μm. The thickness of the substrate and the diameter of the oxide aperture are 200 μm and 400 μm, respectively.

The continuous-wave *V*–*I* characteristics of these three VCSELs are measured under room temperature (RT) and are illustrated in Fig. 5. Compared with the other two VCSELs, the VCSEL with a 300 μm-p-electrode has the highest voltage, which is mainly due to the increased series resistance caused by the reduction in p-electrode diameter. Although it has been demonstrated that the adjustment of p-electrode diameter can effectively suppress the peak of current density distribution near the edge of oxide aperture, reducing the p-electrode too much will increase the series resistance, which will exert a negative effect on the improvement of device performance. A tradeoff must be made to achieve both uniform current density distribution and relative low series resistance.

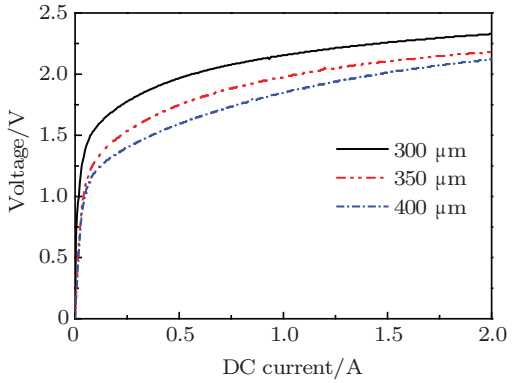

Fig. 5. (color online) Room temperature *V*–*I* characteristics of the VCSELs with three different p-electrode diameters.

Furthermore, by mounting the VCSEL device on the TEC temperature controller, the continuous-wave *L*–*I* characteristics of these three VCSELs are measured under different temperatures and are illustrated in Fig. 6. We can see from Fig. 6 that the values of the RT maximum values of output power of VCSELs with 400-μm- and 350-μm-diameter p-contacts are 0.28 W and 0.3 W, respectively, while the VCSEL with 300-μm-diameter-p-electrode is 0.25 W. When the operating temperature rises to 90 °C, the maximum values of output power of the 400-, 350-, and 300-μm-p-electrode VCSELs decrease by 60.7%, 60%, and 80%. Although series resistance is higher, the *L*–*I* and temperature characteristics of the 350-μm-p-electrode VCSEL are nearly the same as those of the 400-μm-p-electrode VCSEL, this is because the elimination of the local overheating effect caused by the nonuniform current-density distribution partly offsets the influence of increased resistance. On the other hand, due to higher resistance caused by more reducing p-electrode diameter, significant degradations of *L*–*I* and temperature characteristics happen to the 300-μm-p-electrode VCSEL.

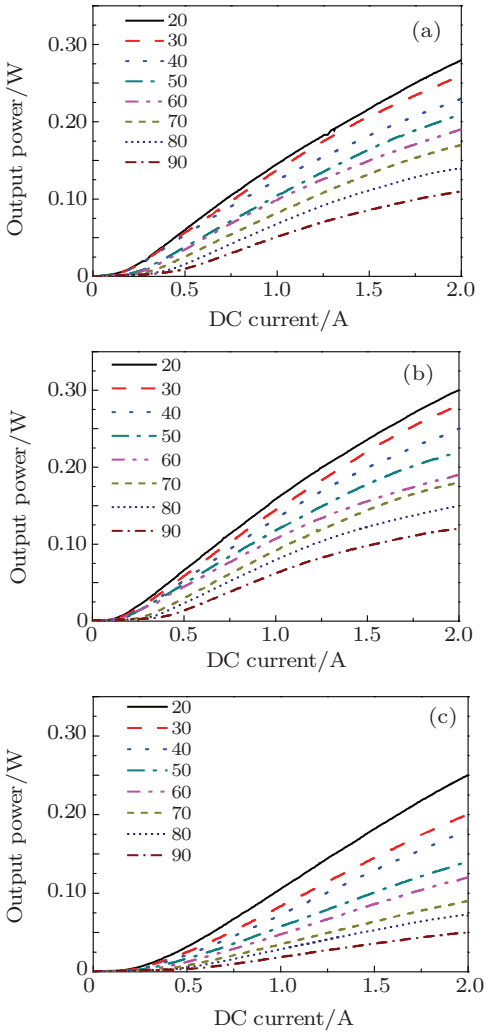

Fig. 6. (color online) The *L*–*I* characteristics of the VCSELs with (a) 400-μm, (b) 350-μm, (c) 300-μm p-electrode diameter under different temperatures.

We measure the far-field distributions of the output of the VCSELs with 400-μm and 350-μm-p-electrode diameters, respectively. The experimental setup is as follows. To eliminate the influence of the self-heating effect, the VCSELs are mounted on a microchannel water cooler to maintain the temperature constant at 20 °C. A receiving screen is placed 2 cm away from the VCSELs and a charge-coupled device (CCD) camera is used to photograph the far-field distributions.

The results of far-field measurements show that there is no side lobe in the far-field distribution of the VCSEL with 350-μm-diameter p-electrode; moreover, its far-field angles are 4.2°, 6.9°, and 9° under the three injected current levels. This is because the smaller diameter of the p-contact effectively improves the current-density distribution in the active region and, hence, lowers the divergence. On the contrary, the current-density peak near the edge of the oxide aperture causes a ring-shaped distribution in the far field of the VCSEL with

a 400-μm-diameter p-electrode, as shown in Fig. 7. Thus, the optimization of the current-density distribution effectively improves the far-field distribution without degradation of the *L–I* characteristics.

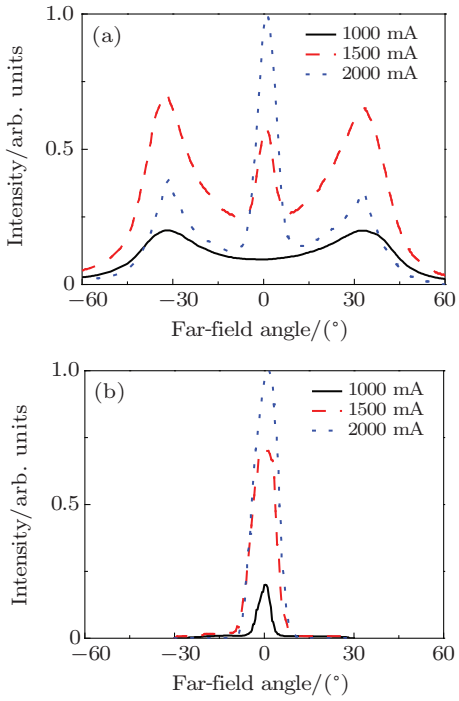

Fig. 7. (color online) Measured far-field distributions of VCSELs with (a) 400 μm-p-electrode (b) 350 μm-p-electrode.

Because the spontaneous emission is directly related to the current-density distribution within the active region, measuring the spontaneous-emission near-field distribution will be a good approach to revealing the current-density distribution.[24] To further investigate the difference in current-density distribution between these two VCSELs, the near-field distributions of these devices are measured below the threshold level. The only difference between the VCSEL near-field below threshold and that above threshold is the optical intensity. Thus, the near-field distribution below the threshold will reveal the same pattern of current density distribution as above the threshold. Another reason for testing the VCSEL devices below the threshold is to avoid the saturation of the CCD camera and obtain the near-field distribution exactly. Here we choose the Ophir–Spiricon^{TM} SP620U CCD camera combined with a 4× microscope to image the near fields of the VCSEL devices. By using the BeamGage^{TM} software, the 2D or 3D map of the near-field can be acquired. The injected current is 0.3 A, which is just below the threshold currents of these two VCSELs. The measured spontaneous-emission near-field distributions are shown in Fig. 8.

As seen from Fig. 8, in the near field of the VCSEL with a 400-μm-diameter p-contact, there is a ring-shaped distribution, which implies nonuniformity of the current-density distribution. In contrast, there is no ring-shaped distribution in the near field of the VCSEL with 350-μm-diameter p-contact; this means that the current-density distribution is optimized.

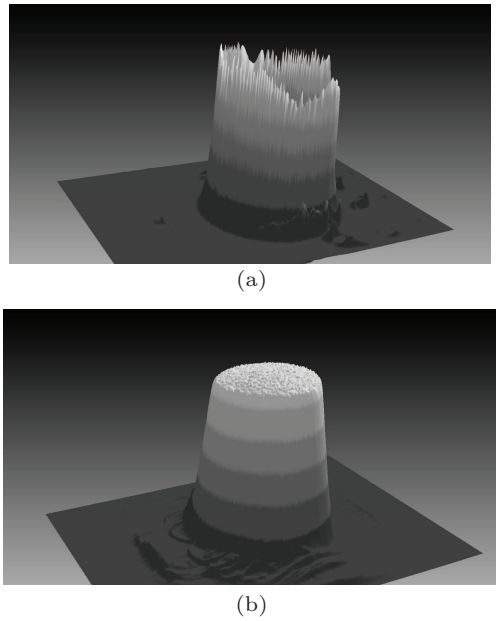

Fig. 8. Spontaneous-emission near-field distributions of VCSELs with (a) 400-μm-diameter p-electrode and (b) 350-μm-diameter p-electrode.

5. Conclusions

The output performance of the 980-nm broad-area VCSEL is improved by optimizing the p-electrode diameter. The simulation results show that the current-density distribution within the active region of the VCSEL is dependent on the p-electrode diameter rather than the diameter of the oxide aperture. Appropriate optimization of the p-electrode can facilitate the uniform current-density distribution in the active region, which will further improve the output performance of the VCSEL. Our experimental investigations show that the series resistance is increased by the adjustment of the p-electrode, however, appropriate p-electrode adjustment can eliminate the nonuniform current density distribution and the following self-heating effect, which will compensate the negative effects of increased resistance. Thus, improved current density distribution could be achieved without significantly degrading the *L–I–V* and temperature characteristics. The divergence angle of the current-density-optimized VCSEL is much smaller than that of the VCSEL with unoptimized current density. The measurements of the near-field distributions of these VCSEL devices further confirm the simulation results.

References

[1] Jewell J 1990 *Laser Focus World* 151
[2] Morgan R A 1997 *SPIE* **3003** 14
[3] Blokhin S A, Karachinsky L Y, Novikov I I, Gordeev N Y, Sakharov A V, Maleev N A, Kuzmenkov A G, Shernyakov Y M, Maximov M V, Kovsh A R, Mikhrin S S, Shchukin V A, Ledentsov N N, Ustinov V M and Bimberg D 2008 *IEEE J. Quantum Electron.* **44** 724
[4] Yue A W, Shen K, Shi J and Wang R F 2004 *Chin. Phys. Lett.* **21** 81

[5] Wang T X, Guan B L, Guo X and Shen G D 2009 *Acta Phys. Sin.* **58** 1694 (in Chinese)
[6] Michalzik R, Grabherr M, Jaeger R, Miller M and Ebeling K J 1998 *SPIE* **3419** 187
[7] Grabherr M, Miller M, Jager R, Martin U, Unold H J and Ebeling K J 1999 *IEEE J. Sel. Topic. Quantum Electron.* **5** 495
[8] Seurin J F, Ghosh C L, Khalfin V, Miglo A, Xu G Y, Wynn J D, Pradhan P and D'Asaro L A 2008 *SPIE* **6876** 68760
[9] Sun Y F, Ning Y Q, Li T, Qin L, Yan C L and Wang L J 2007 *J. Lumin.* **122–123** 886
[10] Seurin J F, Xu G Y, Miglo A, Wang Q, Van Leeuwen R, Xiong Y H, Zou W X, Li D Z, Wynn J D, Khalfin V and Ghosh C 2012 *SPIE* **8276** 827609
[11] Moench H, Dumoulin R, Gronenborn S, Gu X, Heusler G, Kolb J, Miller M, Pekarski P, Ploomann-Restsch J, Pruijmboom A and Stroesser M 2012 *SPIE* **8276** 82760B
[12] Li H Q, Zhang J, Cui D F, Xu Z Y, Ning Y Q, Yan C L, Qin L, Liu Y, Wang L J and Cao J L 2004 *Acta Phys. Sin.* **53** 2986 (in Chinese)
[13] Eliseev P G, Glebov A G and Osinski M, 1997 *IEEE J. Sel. Topic. Quantum Electron.* **3** 499
[14] Angelos C, Hinckley S, Michalzik R and Voignier V 2004 *SPIE* **5277** 261
[15] Yan C L, Ning Y Q, Qin L, Cui D F, Liu Y, Sun Y F, Jin Z H, Li H Q, Tao G T, Wang C, Wang L J and Jiang H L 2005 *IEEE Photon. Tech. Lett.* **17** 1599
[16] Piprek J, Mehta M and Jayaraman V 2004 *SPIE* **5349** 375
[17] Maslov A V and Miyawaki M 2011 *IEEE J. Quantum Electron.* **47** 238
[18] Choi J H, Wang L, Bi H and Chen R T 2006 *IEEE J. Quantum Electron.* **12** 1060
[19] Santschi R, Meier H and Odermatt S 2008 *SPIE* **6889** 68890I
[20] Wang J, Savidis I and Friedman E G 2011 *Microelectron. J.* **42** 820
[21] Zhang Y, Ning Y Q, Qin L, Wang Y, Cui J J, Liu G Y, Zhang X, Wang Z F, Sun Y F, Liu Y and Wang L J 2010 *Appl. Opt.* **49** 3793
[22] Zhang X, Ning Y Q, Zeng Y G, Zhang J L, Fu X H, Qin L, Liu Y, Tong C Z and Wang L J 2012 *IEEE J. Quantum Electron.* **48** 42
[23] Winston D 1996 *Physical Simulations of Optoelectronic Semiconductor Devices* (Ph. D. Thesis) (University of Colorado)
[24] Ackemann T, Barland S, Cara M, Balle S, Tredicce J R, Jäger R, Grabherr M, Miller M and Ebeling K J 2000 *J. Opt. B: Quantum Semiclass. Opt.* **2** 406